



Basics of magnetic resonance imaging and quantitative parameters T1, T2, T2*, T1rho and diffusion-weighted imaging

Suraj D. Serai^{1,2}

Received: 12 November 2020 / Revised: 18 January 2021 / Accepted: 1 March 2021 / Published online: 15 April 2021
© The Author(s), under exclusive licence to Springer-Verlag GmbH Germany, part of Springer Nature 2021

Abstract

Magnetic resonance imaging is widely available and accepted as the imaging method of choice for many pediatric body imaging applications. Traditionally, it has been used in a qualitative way, where the images are reported non-numerically by radiologists. But now MRI machines have built-in post-processing software connected to the scanner and the database of MR images. This setting enables and encourages simple quantitative analysis of MR images. In this paper, the author reviews the fundamentals of MRI and discusses the most common quantitative MRI techniques for body imaging: T1, T2, T2*, T1rho and diffusion-weighted imaging (DWI). For each quantitative imaging method, this article reviews the technique, its measurement mechanism, and selected clinical applications to body imaging.

Keywords Magnetic resonance imaging · Mapping · Quantitative · Relaxation · System components

Introduction

Magnetic resonance imaging (MRI), a non-ionizing radiation modality, relies on magnetic fields for image formation. It is a tomographic imaging technique, acquiring data in multiple thin slices or sections. These sections can be acquired in any orientation, including oblique planes. An MRI machine comprises four main components (Figs. 1 and 2). The first is a magnet powerful enough to generate the strong static magnetic field (denoted by B_0) that is required to induce the proton nuclear polarization. The second is the radiofrequency (RF) system that generates the required alternating magnetic field (B_1) at the resonant frequency and detects the MR signal that is returned from the tissue sample or the patient. The third component is the set of gradient systems (oriented orthogonally in X, Y and Z directions) that generates the required linear magnetic field variations, which are then superimposed upon B_0 and are used to spatially encode the MR signal. In clinical MR scanners, the three gradient sets and whole-body

RF coils are typically concentrically positioned inside the bore of the magnet. Finally, the fourth component consists of computers that provide the user interface, perform the analog-to-digital conversion of the collected signals from the patient, and generate images that can be displayed and interpreted on the console. The computer systems can be programmed to generate quantitative relaxation maps to be displayed on the scanner console after acquisition. The benefits of quantification are that the fundamental research into biological changes in diseases and their response to potential treatments can proceed in a more accurate and precise way.

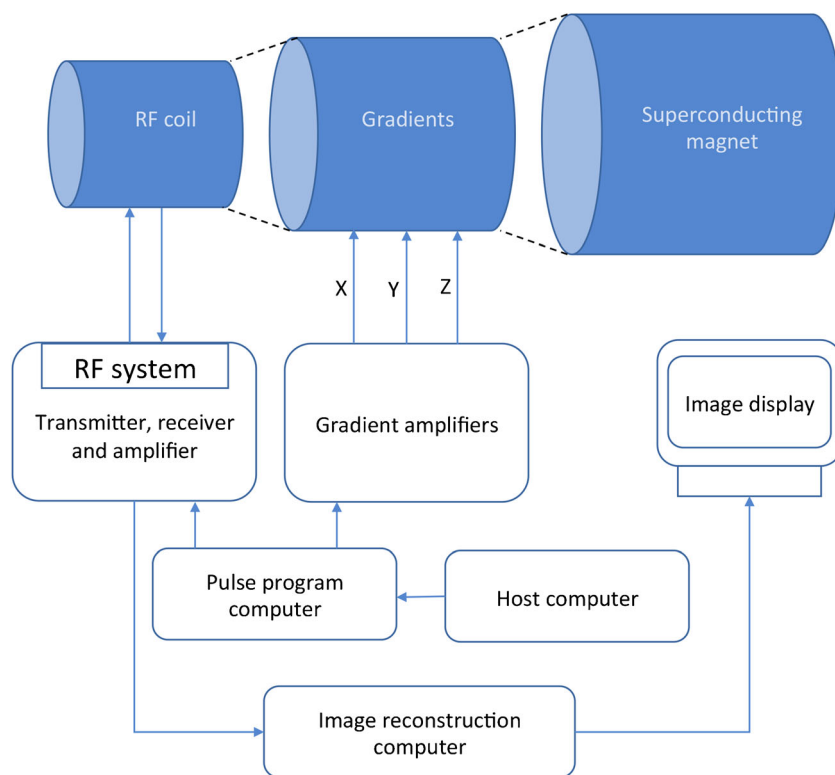
A typical adult is composed of approximately 60% to 70% water [1, 2]. Clinical MRI primarily utilizes the nucleus of hydrogen, i.e. protons. The physical basis of MRI centers around the concept of nuclear spins of proton molecules, and their associated angular momentum and magnetic moment [3]. This magnetic moment is the strength and orientation of the proton's magnetic field, and it interacts with the magnetic fields of the MRI systems. For practical clinical imaging application, the nuclei used for MRI are hydrogen nuclei because of the large natural abundance of the water in human biological systems. As the hydrogen protons precess at a specific frequency, they interact with a matching, i.e. resonant, external alternating magnetic field. Hydrogen nuclei possess intrinsic spin angular momentum, and a magnetic dipole moment that is parallel to the spin vector. In the presence of an external static magnetic field, B_0 , the magnetic moments

✉ Suraj D. Serai
serais@chop.edu

¹ Department of Radiology, Children's Hospital of Philadelphia, 3401 Civic Center Blvd., Philadelphia, PA 19104, USA

² Perelman School of Medicine at the University of Pennsylvania, Philadelphia, PA, USA

Fig. 1 Block diagram shows an overview of an entire MR system. *RF* radiofrequency



of hydrogen nuclei precess with two possible orientations, either parallel or anti-parallel to the static magnetic field, and a net alignment of nuclei exists parallel to the direction of the externally applied field (B_0).

where γ is the gyromagnetic ratio, 42.5 MHz/tesla (T). Therefore, the precession frequency for hydrogen nuclei for 1.5 T is approximately 64 MHz and for 3 T is 128 MHz.

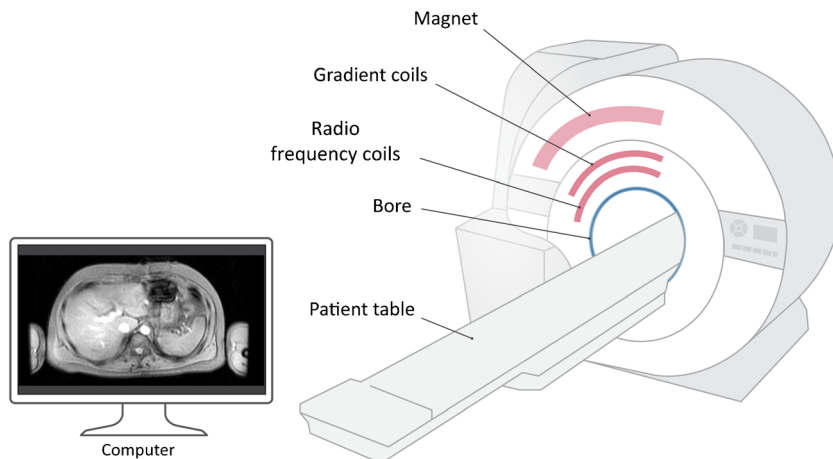
Larmor frequency

Individual hydrogen nuclei precess around the B_0 field at a resonance frequency known as the Larmor frequency (Fig. 3). The Larmor frequency, ω_0 , of the net magnetization vector generally occurs in the RF range of the electromagnetic spectrum and is related to the external magnetic field as $\omega_0 = \gamma B_0$,

Radiofrequency excitation and magnetic resonance signal detection

The strength of a magnetic field is measured in tesla. A standard 1.5-T system provides a magnetic field of about 30,000 times that of the Earth's magnetic field. If there is no external, applied magnetic field, magnetic moments of the hydrogen nuclei are randomly oriented and do not form any coherent

Fig. 2 Schematic of a clinically used MRI scanner



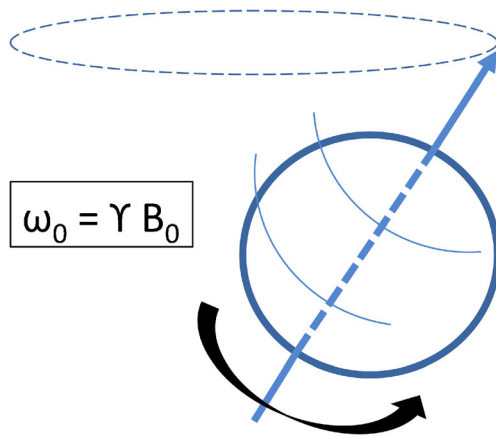


Fig. 3 The frequency of hydrogen nuclei precession is known as the Larmor frequency (ω_0), where γ is the gyromagnetic ratio (42.5 MHz/T) and B_0 is the external magnetic field

magnetization. However, when the hydrogen nuclei are placed in the presence of a strong static magnetic field (B_0) such as a clinical MRI scanner of field strength 1.5 T or 3.0 T, the nuclei split into two energy states, either aligned parallel to the magnetic field B_0 (which is also called a “spin-up” state) or aligned antiparallel to B_0 (also called a “spin-down” state). The spin-up state has a slightly lower energy level as compared to the spin-down state and is therefore preferred. This slight difference in the spin states (0.001%) results in an overall net magnetization (M) aligned in the same direction as the main magnetic field B_0 .

To create an MR signal, we excite the spins out of resting equilibrium, i.e. we tip the net magnetization away from the static magnetic field B_0 . To detect the signal from the hydrogen nuclei in the tissues in the presence of a strong static magnetic field, we introduce an additional external field (denoted by B_1) at the resonant Larmor frequency that can affect the net magnetization vector, causing it to rotate into a plane orthogonal to its original orientation. The rotated magnetization vector continues to precess around the main magnetic field. The precession of the magnetization vector in the transverse plane can be detected by an RF coil tuned to the resonant frequency.

Radiofrequency coils are the “antennae” of the MRI system, transmitting the RF signal from the system to the patient and receiving the return signal from the patient back to the system. RF coils can be operated in a receive-only mode, in which case the inherent body coil is used as a transmitter; or the RF coils can be both transmit and receive. The purpose of the RF transmit coil is to create a time-varying B_1 field at right angles to B_0 that could be linearly or circularly polarized. Generally, a large-diameter birdcage “body” coil is used because this creates the most spatially uniform B_1 field. The closer the receiving coil is to the source of the MR signal, the better the signal-to-noise ratio (SNR). Receiver coils generally comprise arrays of smaller individual coils or elements; however, each individual coil element has a limited depth

penetration. Multiple arrays of coils, termed “phased-array coils,” can be used together to achieve a higher coverage. The multiple coils are electronically decoupled from one another so that they don’t appear as just a single large coil. The images from individual coils are independently reconstructed and then grouped together to create the final image.

An RF pulse of amplitude B_1 , termed an “excitation pulse,” is applied for a certain time duration to tip the magnetization at an angle away from the B_0 field. The precessing transverse magnetization induces a voltage in the receiver RF coil; this induced voltage is known as the free induction decay. After the pulse, the magnetization returns to thermal equilibrium by processes known as MR relaxation [4]. To fully encode the spatial information within the field of view (FOV), pulse sequences must be iterated numerous times. The time between successive iterations of a pulse sequence is known as the repetition time (TR). The time between the application of the initial RF pulse and the middle of the detected echo is known as the echo time (TE).

Signal relaxation mechanisms

Once the RF pulse is turned off, the net magnetization continues to precess as it returns to its thermal equilibrium state. During this time, two types of relaxation occur: T1 (longitudinal or spin lattice) and T2 (transverse or spin/spin). One attribute that makes T1 and T2 so valuable for determining the signal in MRI is their sensitivity to the presence and type of tissue. It is this tissue dependence property that gives MR its excellent soft-tissue contrast.

T1 relaxation

T1 relaxation describes the recovery of the longitudinal magnetization back to thermal equilibrium following a perturbation by an RF pulse (Fig. 4). The longitudinal component regrows along the z-direction with a time constant T1 [4]. In other words, after the RF pulse is turned off, the protons that were disturbed give their energy to the surrounding environment and return back to their original equilibrium state, realigning with the magnetic field. Hence T1 relaxation is also called longitudinal relaxation. Furthermore, because T1 relaxation involves the loss of energy that was put into the spin system by the RF pulse, it is also referred to as spin-lattice relaxation, the “lattice” consisting of surrounding macromolecules. This loss of energy is stimulated by the fluctuating magnetic fields associated with the dipole–dipole interactions of neighboring magnetic moments. T1 relaxation can only occur when these magnetic field fluctuations occur at the resonant frequency. The rate at which the spin magnetization (M_z) recovers to M_0 at time t is called T1 relaxation time.

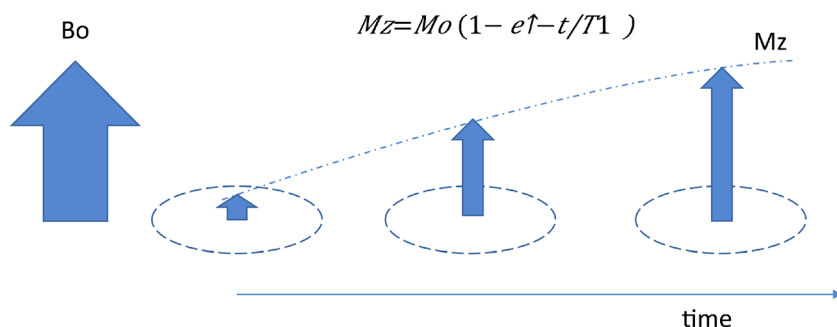


Fig. 4 The rate at which the spin magnetization (M_z) at time t recovers to the original magnetization (M_0) at time $t=0$ is called T1 relaxation time, where B_0 is the external magnetic field. T1 relaxation time measured is

The magnetization M_z can be expressed as the following equation:

$$M_z = M_0 \left(1 - e^{-\frac{t}{T_1}} \right)$$

So T1 relaxation time is defined by the time it takes for the longitudinal magnetization to grow to about 63% of its final value (Fig. 4). T1 mapping is a method of quantifying the T1 value of the tissue across the field of view. T1 mapping also refers to pixelwise illustrations of T1 relaxation times on a map. This parametric map can be calculated from two or more images of the same tissue.

How to measure T1 relaxation time for body imaging

A preferred method of measuring T1 relaxation in body imaging is the Look-Locker method, which is based on the principle that we need not wait for the net magnetization vector to equilibrate in order to measure T1. Instead, we use an RF pulse with a small flip, which can be repeatedly applied. The acquisition pulse sequence is designed to generate a train of signals that gradually approaches a steady-state recovery. The recovery curve measured by this technique can be fitted to an exponential curve to provide an effective T1 measurement. In clinical settings, liver T1 is measured using a modified Look-Locker inversion recovery (MOLLI) pulse sequence that allows measurement of T1 times in a single breath-hold. This has become the most popular T1-mapping method for abdomen and cardiac imaging [5–7]. The general principle of T1 mapping is to acquire multiple images with different T1 weightings and to fit the signal intensities of the images to the equation of T1 relaxation (Fig. 5). T1 mapping using MOLLI-based techniques is being applied and published widely in a substantial number of cardiac and liver applications [6–10]. T1 relaxation values for tissues can be estimated by fitting the data to the following equation:

$$S = S_0 \left(1 - A e^{-\frac{t}{T_1}} \right)$$

the time for the longitudinal magnetization to re-grow to about 63% of its final value (the flipped nuclei realign with the main magnetic field)

where S is the signal intensity measured at each inversion time (TI) value, S_0 is the initial signal intensity at time, $t=0$, and A is a constant.

Applications of T1 relaxation measurements in body imaging

The longitudinal T1 relaxation time constant of the tissue is altered in various disease states because of increased water content or other changes to the local molecular environment [6]. The two most important biological determinants of an increase in T1 relaxation times are edema (increase of tissue water, e.g., in acute infarction or inflammation) and increase of interstitial space (e.g., fibrosis or infarction [scar] or cardiomyopathy, and in amyloid deposition). There is more than one flavor of MOLLI that can be used for body MRI applications [11, 12]. T1 maps generated from current clinically approved MOLLI acquisitions are typically derived from cardiac-triggered single-shot balanced steady-state free precession acquisitions. This acquisition technique allows imaging of one anatomical level during a single breath-hold [5, 8, 10]. Other techniques are also available, including a volumetric method for T1 measurements using a spiral k-space trajectory to cover the entire liver in a single breath-hold [13].

T1 mapping has the potential to detect and quantify diffuse fibrosis at an early stage [9, 14]. As a result of oblique angle imaging of the myocardium during cardiac imaging, T1 mapping of the liver can be performed without additional time and within the same field of view (Fig. 6). Kazour et al. [10] have used T1 mapping in cardiovascular MR to assess for congestive hepatopathy. Liver T1 mapping has been shown to positively correlate with MR elastography-derived liver stiffness [7, 15]. Banerjee et al. [5] have shown iron-corrected T1 (cT1) relaxometry/mapping to correlate with liver fibrosis and inflammation. In this proprietary method, T1 relaxation values are corrected for presence of iron or T2* using a patented formula ($cT1 = T1 - 420 + (20 \times T2^*)$) [16]. T1 mapping is feasible even in children with severe renal impairment in whom gadolinium-based contrast agents are contraindicated. Primary advantages of T1 mapping for assessing myocardial or liver fibrosis include its noninvasive nature and lack of need

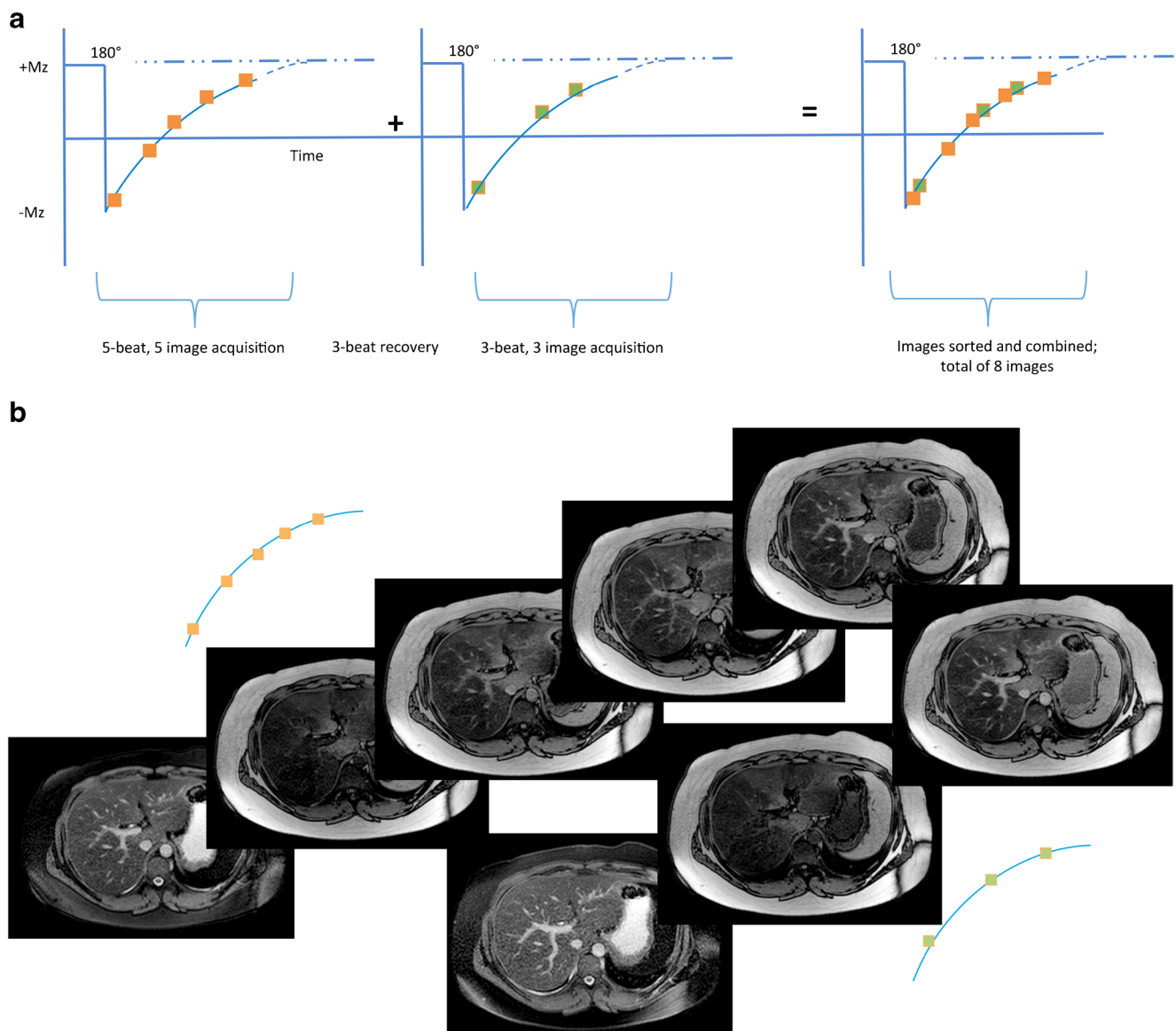


Fig. 5 T1 mapping. **a** Acquisition strategy for the modified Look-Locker sequence (MOLLI). In this example, after a 180° inversion pulse, images are acquired in diastole over five heartbeats, followed by a rest period of three heartbeats. Then, after another inversion, another three images are acquired with slightly offset inversion times (TI) to sample more points along the inversion recovery curves. Based on the number of heartbeats

for acquiring images after each inversion pulse, and on a rest period of three heartbeats between the two cycles, this MOLLI acquisition scheme is termed 5(3)3. **b** Representative images acquired axially in a 14-year-old boy are sorted in order of increasing TI, and the signal intensity in each pixel is then measured and used to fit to the T1 recovery curve equation

for additional hardware, such as the active and passive drivers required for MR elastography (Fig. 7) [17, 18].

T2 relaxation

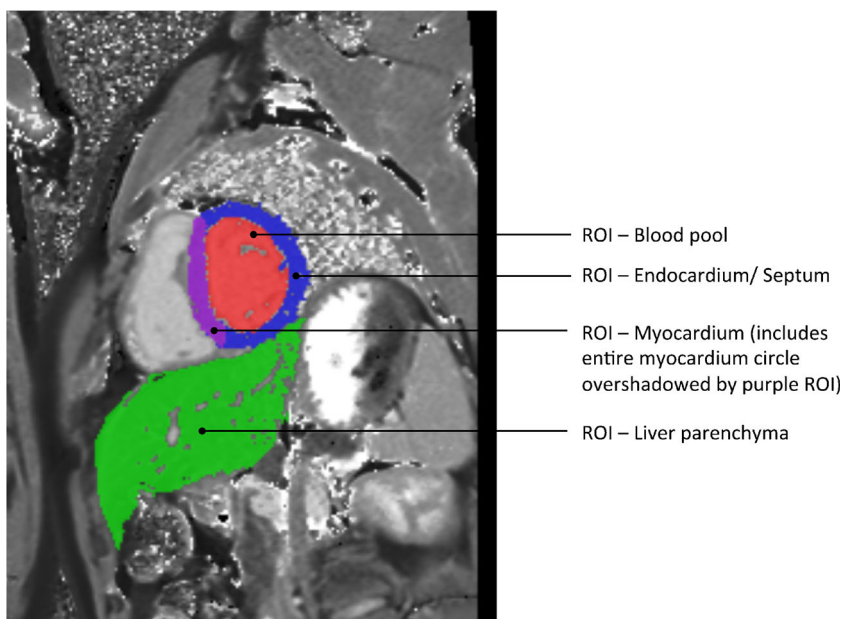
T2 relaxation results in the loss of transverse magnetization caused by interactions between the magnetic fields of neighboring hydrogen nuclei (Fig. 8). It is not an energy loss process like T1 but is a loss of phase coherence within the spin system. This process, also known as spin-spin relaxation, leads to the destruction of transverse magnetization and causes the magnetic moments of the tissue to dephase. Different

tissues in the body have different T2 values. T2 relaxation time is measured as the time required for the transverse magnetization to decay to approximately 37% of its initial value.

How to measure T2 relaxation time for body imaging

T2 mapping is a method of measuring the T2 value of the tissue. T2 relaxation time can be calculated using a T2 sequence with different echo times (TEs). The most fundamental sequence for T2 mapping is signal measured with spin-echo techniques (multiple sequences with different TE values) [19]. Other 2-D sequences have been used, such as multi-echo

Fig. 6 Representative T1 map of the myocardium and liver in an 11-year-old boy referred for cardiac MR imaging generated in the same short-axis view during a cardiac image acquisition. ROI region of interest



spin echo (MSME) and fast spin echo (FSE) [19]. Synthetic MRI is another quantitative method in which a single saturation recovery turbo spin-echo sequence is used to estimate T2 transverse relaxation [20]. T2 relaxation values for tissues can be estimated by fitting the data to the following equation using a mono-exponential decay curve:

$$S(TE) = S_0 e^{-\left(\frac{TE}{T_2}\right)}$$

where S(TE) is the signal intensity measured at each TE and S_0 is the initial signal intensity at time $t=0$.

Applications of T2 relaxation measurements in body imaging

Applications of T2 relaxations are described together with those for T2* relaxation in the “Applications of T2 and T2* relaxation measurements in body imaging” subsection.

T2* relaxation

The spins in the transverse magnetization plane dephase because of the intrinsic spin-spin interactions (T2). Additional dephasing of the magnetization is caused by magnetic susceptibility sources and magnetic field inhomogeneity. Because of this extra phase dispersion, the decay time of the transverse magnetization is shortened and given as T2*.

How to measure T2* relaxation time for body imaging

T2* of a tissue is measured with gradient recalled echo (GRE)-based sequences (in body imaging this is

typically a fast single-breath-hold acquisition sequence). Similar to T2 measurements, T2* signal can be measured from the multiple echo times of a GRE-based acquisition sequence, and T2* value can be estimated by fitting the data to the following equation using a mono-exponential decay curve:

$$S(TE) = S_0 e^{-\left(\frac{TE}{T_2^*}\right)}$$

where S(TE) is the signal intensity measured at each TE and S_0 is the initial signal intensity at time $t=0$ (Fig. 9).

Applications of T2 and T2* relaxation measurements in body imaging

Liver T2 and T2* quantitative methods are routinely used clinically for body liver iron assessments (Fig. 10) [21–24]. Measured mean cardiac T2*, liver T2 and liver T2* can be converted to cardiac iron or liver iron concentrations (LIC) by published formulae [23, 25, 26].

$$\begin{aligned} \text{Cardiac iron concentration} &= 45/(T_2^*)^{1.22} \\ \text{LIC (using } T_2^*) &= 0.0254/T_2^* + 0.202 \\ \text{LIC (using } T_2) &= \left(29.75 - \sqrt{900.7 - 2.283/T_2}\right)^{1.424} \end{aligned}$$

In a study of 123 patients with MRI and biopsy performed within a 6-month period, Guimaraes et al. [27] showed a significant increase in T2 measurements with increasing fibrosis stages using mono-exponential curve fitting. In a different study of 139 patients, Hoffman et al. [15] showed that liver

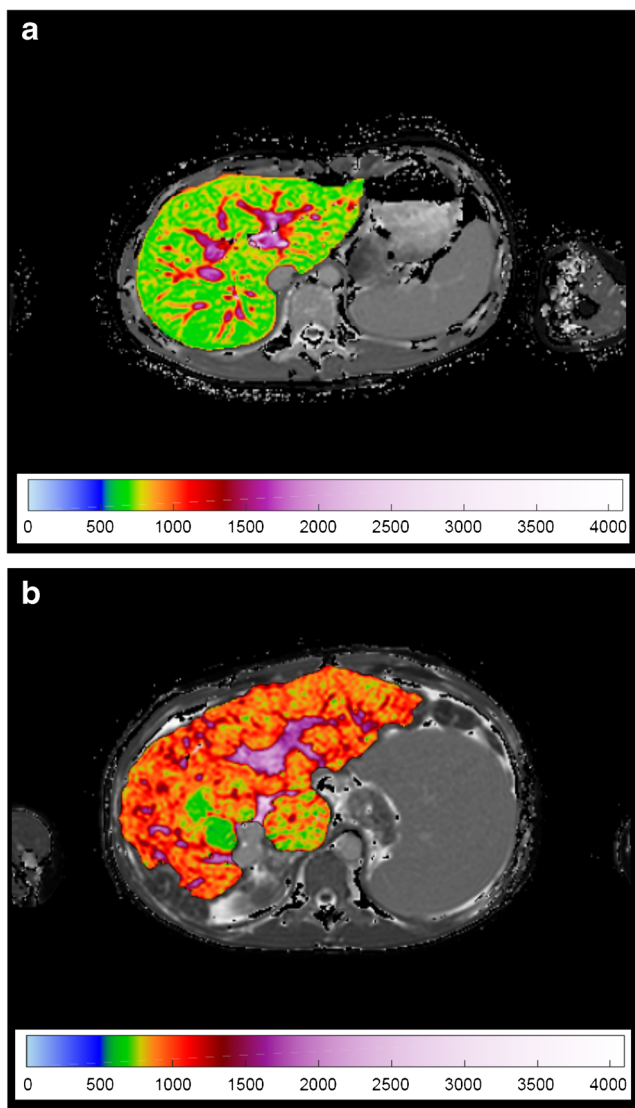


Fig. 7 Iron-corrected T1 (cT1) liver mapping. **a, b** Axial iron-corrected T1 map of a 9-year-old boy with normal liver (mean=704 ms) (**a**) as compared to cT1 map of a 16-year-old boy with primary sclerosing cholangitis (mean=1,048 ms) (**b**). Images were acquired in axial orientation

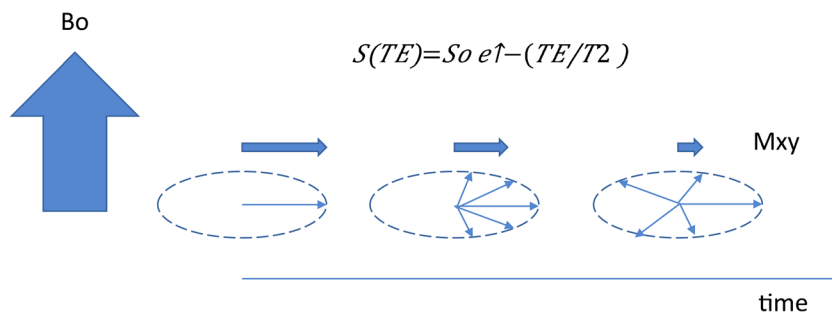


Fig. 8 T2 relaxation. Following turning off of the radiofrequency pulse, differences in magnetic fields experienced by the spins cause them to precess at slightly different frequencies and fan out about the transverse plane. T2 relaxation time is the time for the transverse magnetization to

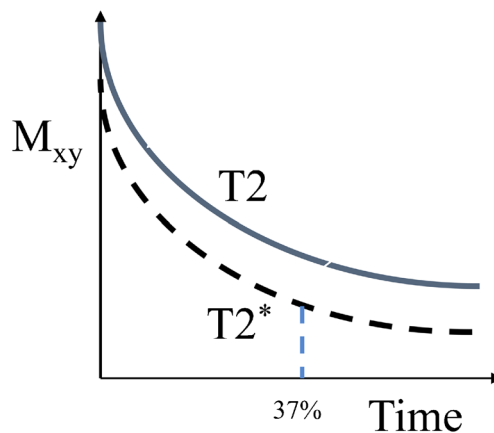


Fig. 9 T2* measurement. While T2 relaxation time is the “true” T2 caused by spin-spin molecular interactions, T2* relaxation time is the “observed” T2, reflecting true T2 as well as the effect of magnetic and gradient inhomogeneity. T2 or T2* as measured is the time required for the transverse magnetization to fall to approximately 37% of its initial value

T1 and T2 mapping had a positive correlation with MR elastography, which is a stiffness-based biomarker of liver fibrosis. These findings support the potential utility of T2 mapping in quantifying liver fibrosis. In musculoskeletal imaging, T2 mapping technique has shown potentiality to evaluate the quality of the cartilage composition because the transversal relaxation time (T2) reflects the ability of proton molecules to move and to exchange energy inside the cartilaginous matrix [28, 29]. Each variation of matrix content (water, proteoglycan and collagen) and each modification of the organization of the collagen network can induce T2 variations that can be measured quantitatively for early disease detection and treatment follow-up [30].

T1rho concept

T1rho, or spin-lock T1 relaxation time, is the time constant for magnetic relaxation under continuous RF irradiation. When an RF pulse is delivered at moderate

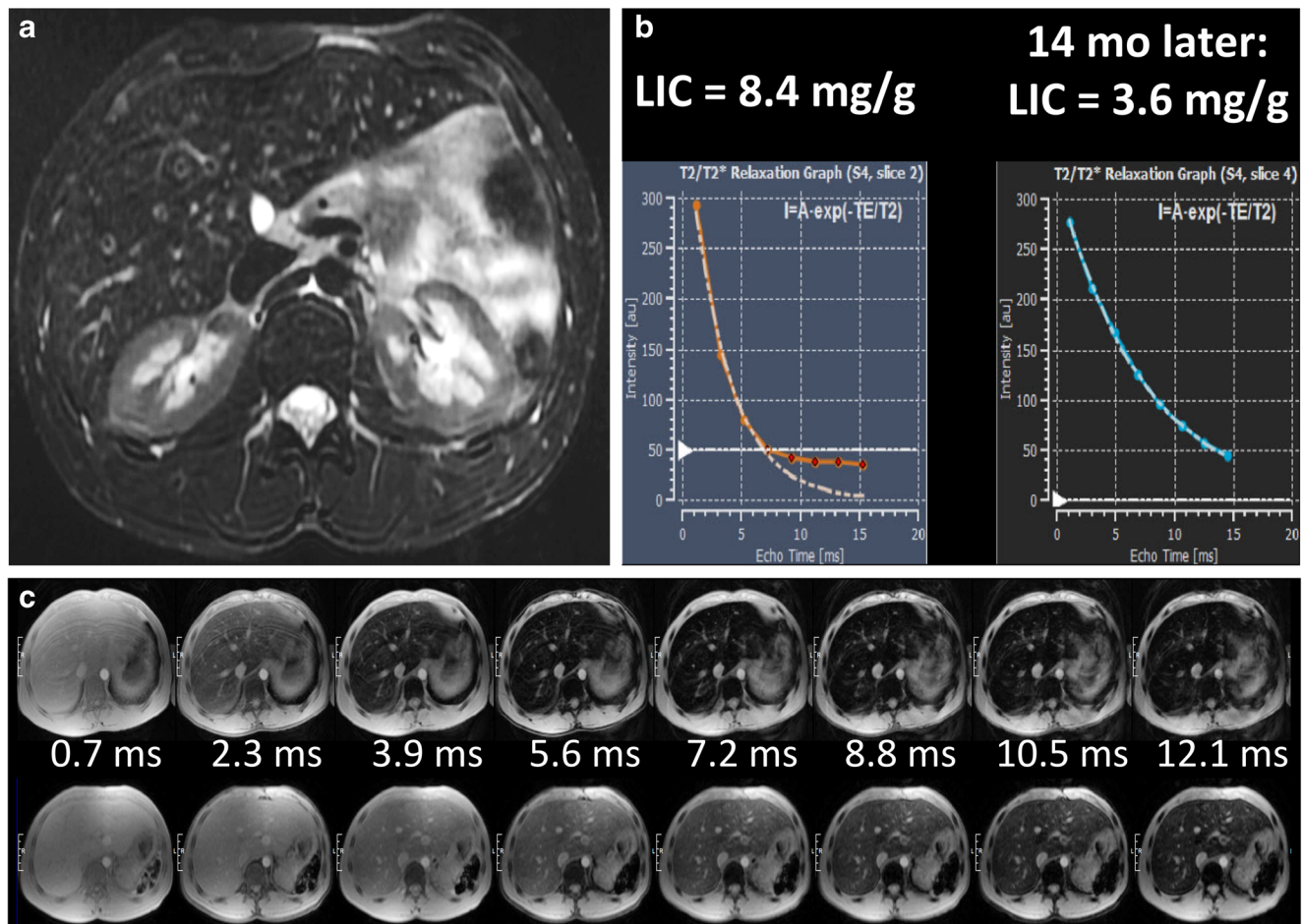


Fig. 10 T2 and T2* applications in liver imaging. **a** Axial T2-W fat-suppressed MR image in a 16-year-old boy with sickle cell disease who is transfusion-dependent. **b** Liver iron concentration (LIC) measured with T2*-based images is 8.4 mg/g. The same boy was scanned approximately 14 months after chelation therapy, and his estimated LIC was 3.6 mg/g. This is also reflected in the signal intensity of the individual increasing

echoes. *TE* echo time. **c** Top row shows axial images of the liver, which can be seen getting progressively darker with increasing echo images when LIC measured was 8.4 mg/g. Bottom row shows axial images of the same boy with LIC measured at 3.6 mg/g approximately 14 months later after chelation therapy

amplitude ($\sim 10 \mu\text{T}$), it can quench background sources of T2 relaxation in fibrotic tissue, greatly enhancing sensitivity to fibrotic liver disease compared to conventional T2-relaxation mapping. Also known as spin-lattice relaxation time in the rotating frame, this imaging technique measures relaxation time in the presence of a resonant continuous wave radiofrequency pulse that “locks” its magnetization in the transverse plane. T1rho describes the decay of this locked magnetization in the transverse plane and is influenced by the interactions between free water and proton nuclei in large macromolecules, such as collagen and proteoglycans.

How to measure T1rho relaxation in body imaging

T1rho mapping is the most common form of T1rho imaging and has been most intensively used for various applications.

T1rho mapping involves at least two, usually multiple spin-lock times (TSL) at a certain spin-lock frequency to obtain a series of images with different levels of T1rho weighted contrast. Voxel-wise image intensities with different TSLs are then fitted to a mono-exponential decay mathematical model, to calculate the voxel-wise T1rho values, which is called T1rho map.

Applications of T1rho relaxation measurements in body imaging

T1rho mapping has been used in preclinical and research settings to assess for hepatic fibrosis [31–33]. Because liver fibrosis involves the accumulation of extracellular macromolecules, including collagen and proteoglycans, it is hypothesized that T1rho imaging is a direct measure of liver fibrosis and

might be less confounded as compared to stiffness-based measures [14, 18].

In a small study by Rauscher et al. [31], T1rho measurements were made in healthy volunteers and patients with liver cirrhosis. These authors concluded that liver T1rho values were significantly higher in people with liver cirrhosis when compared to healthy individuals. Another study, by Singh et al. [32], which performed T1rho relaxometry in people with varying degrees of liver fibrosis, also confirmed that T1rho measurements increase with increasing histological fibrosis. T1rho has been used extensively to study the musculoskeletal system, including cartilage, meniscus and intervertebral discs. T1rho might be able to distinguish tumors as well as healthy and adipose tissue in the breast [34]. It has been shown to improve delineation of myocardial borders and detect myocardial injuries [35, 36].

Diffusion-weighted imaging

Diffusion-based imaging produces images that are sensitized to the molecular diffusion of water [37]. The basis of the signal measured in a diffusion-weighted image is the random movement of water protons. In a static, homogeneous magnetic field, all hydrogen nuclei precess with the same Larmor frequency. When a gradient (a temporary magnetic field) is turned on, this homogeneity can be dephased and then followed by a gradient in the opposite direction to rephase and restore the signal. The hydrogen molecules that move between the dephasing and rephasing gradients contribute to the diffusion-weighted image. The strength of the diffusion weighting is dependent upon the gradient strength, duration and time between the dephasing and rephasing gradients, called the b value and measured in units of s/mm^2 . The higher the b value, the stronger the diffusion weighting [37]. Strong gradients and high slew rates reduce the diffusion encoding time, which improves the SNR by reducing the TE. High slew rates also enable faster image encoding, which can further reduce TE and help mitigate distortions by shortening the echo spacing.

On clinical scanners, diffusion-weighted imaging (DWI) is typically performed with single-shot k-space trajectories, most commonly using the echoplanar imaging (EPI) technique. In an attempt to accelerate imaging, acquired diffusion images are often under-sampled to reduce the effective echo time and length of echo train. Parallel imaging is used to restore the unaliased images by using spatial information inherent in the coil sensitivity profiles of a multichannel receiver coil. Compressed sensing is being explored in research studies as another way to accelerate diffusion imaging by using a priori information about sparsity patterns to reduce sampling requirements [38–40]. Newer methods are now clinically available that help reduce the number of excitations and diffusion encodings necessary to cover the entire imaging volume, such as simultaneous multi-slice [41].

How to measure apparent diffusion coefficients for body imaging

It is possible to estimate for the physical diffusion coefficient of the image voxel, often referred to as the apparent diffusion coefficient (ADC), because it reflects the average diffusion coefficient in the voxel, affected by biophysical factors and experimental setup. The ADC can be measured from the set of diffusion-weighted images and corresponding b factors. For a successful multiple b values DWI acquisition, it is important to optimize the SNR at each b value. In body imaging, to enable a mono-exponential fit, three to five b values are typically used (Fig. 11). The number of signal averages is usually increased for higher b values so that a DWI with multiple b values can be performed at an acceptable SNR in clinically reasonable scan times. The ADC is calculated by fitting the measured signal intensity to the mono-exponential decay curve of the following equation:

$$S = S_0 e^{-b(\text{ADC})}$$

where S is the signal intensity measured from images at each b value and S_0 is the initial signal intensity at time $t=0$.

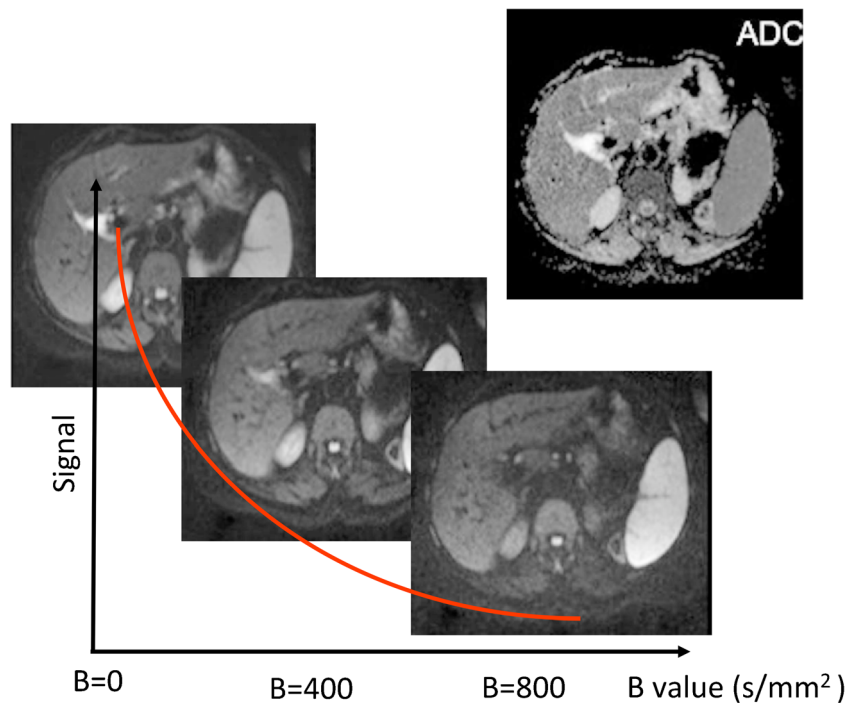
Applications of diffusion-weighted body imaging

In body imaging, DWI has been shown to improve disease assessment in the liver, pancreas, kidney, breast, prostate and kidneys [40, 42–45]. DWI has also shown value in the assessment of tumor response after oncological treatment [46–48]. Various studies have shown that DWI-based ADC values are helpful in early detection and in follow-up of various tumor types [49]. DWI has the potential to assess tissues at a cellular basis and can therefore detect treatment response earlier than other anatomical measures [48]. Change in ADC values often precede changes in tumor size, and the magnitude and temporal evolution of ADC change depends on the mechanism of action of the treatment. A meta-analysis study showed no major differences between DWI and contrast-enhanced T1-W studies using gadolinium-based contrast agents for the detection of liver metastases [50]. In children who cannot receive gadolinium-based contrast agents, DWI can serve as a reasonable alternative to contrast-enhanced studies.

Limitations of quantitative magnetic resonance imaging

The qualitative nature of MR image contrasts and variability in images leads to ambiguity in image interpretation, which is apparent in radiology reports. Additionally, there can be confounding changes in the same anatomical region, adding to the difficulty in image interpretation. The adoption of comprehensive quantitative tissue measurements could help answer complex

Fig. 11 In diffusion-weighted imaging, a progressive decrease in image signal intensity is evident and can be measured with increasing b values, as in these three representative axial images obtained at $b=0$ s/mm², $b=400$ s/mm² and $b=800$ s/mm² in a 14-year-old boy. The signal intensity can be measured and fitted to a mono-exponentially decaying curve to generate an apparent diffusion coefficient (ADC) map (top right)



clinical questions, and MRI-derived quantitative numbers might be used to follow up therapeutic outcomes. However, the inherent speed limitations of MRI preclude widespread clinical adoption of quantitative tissue property measurements. With the availability of faster imaging techniques and rapid gradients, it is now becoming possible to collect quantitative information in a clinical setting. A second barrier to clinical adoption is the lack of standardization and difficulty in reproducibility of quantitative imaging biomarkers. Despite these challenges, it is clear that quantitative-MRI-based measurements have significant potential to impact clinical body imaging.

Conclusion

A growing number of quantitative MR applications for body imaging represents evolutionary change in the use of MR imaging. Quantitative maps improve early detection and staging of chronic diseases and their treatment follow-up. The rapid increase in power and availability of computing technology has enabled MRI manufacturers to provide push-button automatic post-processing and generation of maps on the MR console following acquisition of images. This new ease of access to quantitative maps could provide unique advantages to routine clinical body MR imaging.

Declarations

Conflicts of interest None

References

1. Chumlea WC, Guo SS, Zeller CM et al (1999) Total body water data for white adults 18 to 64 years of age: the Fels longitudinal study. *Kidney Int* 56:244–252
2. Borkan GA, Norris AH (1977) Fat redistribution and the changing body dimensions of the adult male. *Hum Biol* 49:495–513
3. Brown RW, Cheng Y-CN, Haacke EM et al (2014) Classical response of a single nucleus to a magnetic field. In: *Magnetic resonance imaging*, 2nd edn. John Wiley & Sons, Hoboken, pp 19–36
4. Brown RW, Cheng Y-CN, Haacke EM et al (2014) Magnetization, relaxation, and the Bloch equation. In: *Magnetic resonance imaging*, 2nd edn. John Wiley & Sons, Hoboken, pp 53–66
5. Banerjee R, Pavlides M, Tunnicliffe EM et al (2014) Multiparametric magnetic resonance for the non-invasive diagnosis of liver disease. *J Hepatol* 60:69–77
6. Kellman P, Hansen MS (2014) T1-mapping in the heart: accuracy and precision. *J Cardiovasc Magn Reson* 16:2
7. Ramachandran P, Serai SD, Veldtman GR et al (2019) Assessment of liver T1 mapping in Fontan patients and its correlation with magnetic resonance elastography-derived liver stiffness. *Abdom Radiol* 44:2403–2408
8. Dillman JR, Serai SD, Trout AT et al (2019) Diagnostic performance of quantitative magnetic resonance imaging biomarkers for predicting portal hypertension in children and young adults with autoimmune liver disease. *Pediatr Radiol* 49:332–341
9. Everett RJ, Stirrat CG, Semple SI et al (2016) Assessment of myocardial fibrosis with T1 mapping MRI. *Clin Radiol* 71:768–778
10. Kazour I, Serai SD, Xanthakos SA, Fleck RJ (2018) Using T1 mapping in cardiovascular magnetic resonance to assess congestive hepatopathy. *Abdom Radiol* 43:2679–2685
11. Child N, Suna G, Dabir D et al (2018) Comparison of MOLLI, shMOLLI, and SASHA in discrimination between health and disease and relationship with histologically derived collagen volume fraction. *Eur Heart J Cardiovasc Imaging* 19:768–776

12. Roujol S, Weingärtner S, Foppa M et al (2014) Accuracy, precision, and reproducibility of four T1 mapping sequences: a head-to-head comparison of MOLLI, ShMOLLI, SASHA, and SAPPHERE. *Radiology* 272:683–689
13. Chen Y, Lee GR, Aandal G et al (2016) Rapid volumetric T1 mapping of the abdomen using three-dimensional through-time spiral GRAPPA. *Magn Reson Med* 75:1457–1465
14. Serai SD, Trout AT, Miethke A et al (2018) Putting it all together: established and emerging MRI techniques for detecting and measuring liver fibrosis. *Pediatr Radiol* 48:1256–1272
15. Hoffman DH, Ayoola A, Nickel D et al (2020) T1 mapping, T2 mapping and MR elastography of the liver for detection and staging of liver fibrosis. *Abdom Radiol* 45:692–700
16. Banerjee R, Pavlides M, Barnes E (2014) Method and apparatus for non-invasive detection of inflammation of a visceral organ. Google Patents. <https://patents.google.com/patent/WO2015144916A1/en>. Accessed 10 Feb 2021
17. Serai SD, Towbin AJ, Podberesky DJ (2012) Pediatric liver MR elastography. *Dig Dis Sci* 57:2713–2719
18. Serai SD, Trout AT, Sirlin CB (2017) Elastography to assess the stage of liver fibrosis in children: concepts, opportunities, and challenges. *Clin Liver Dis* 9:5–10
19. Mosher TJ, Dardzinski BJ (2004) Cartilage MRI T2 relaxation time mapping: overview and applications. *Semin Musculoskelet Radiol* 8:355–368
20. Fritz J (2019) T2 mapping without additional scan time using synthetic knee MRI. *Radiology* 293:631–632
21. Barrera CA, Khrichenko D, Serai SD et al (2019) Biexponential R2* relaxometry for estimation of liver iron concentration in children: a better fit for high liver iron states. *J Magn Reson Imaging* 50:1191–1198
22. Barrera CA, Otero HJ, Hartung HD et al (2019) Protocol optimization for cardiac and liver iron content assessment using MRI: what sequence should I use? *Clin Imaging* 56:52–57
23. Serai SD, Fleck RJ, Quinn CT et al (2015) Retrospective comparison of gradient recalled echo R2* and spin-echo R2 magnetic resonance analysis methods for estimating liver iron content in children and adolescents. *Pediatr Radiol* 45:1629–1634
24. Serai SD, Trout AT, Fleck RJ et al (2018) Measuring liver T2* and cardiac T2* in a single acquisition. *Abdom Radiol* 43:2303–2308
25. Wood JC (2014) Use of magnetic resonance imaging to monitor iron overload. *Hematol Oncol Clin North Am* 28:747–764
26. Wood JC, Enriquez C, Ghugre N et al (2005) MRI R2 and R2* mapping accurately estimates hepatic iron concentration in transfusion-dependent thalassemia and sickle cell disease patients. *Blood* 106:1460–1465
27. Guimaraes AR, Siqueira L, Uppal R et al (2016) T2 relaxation time is related to liver fibrosis severity. *Quant Imaging Med Surg* 6:103–114
28. Kijowski R, Blankenbaker DG, Munoz Del Rio A et al (2013) Evaluation of the articular cartilage of the knee joint: value of adding a T2 mapping sequence to a routine MR imaging protocol. *Radiology* 267:503–513
29. Kim H, Serai S, Merrow A et al (2014) Objective measurement of minimal fat in normal skeletal muscles of healthy children using T2 relaxation time mapping (T2 maps) and MR spectroscopy. *Pediatr Radiol* 44:149–157
30. Welsch GH, Hennig FF, Krinner S, Trattnig S (2014) T2 and T2* mapping. *Curr Radiol Rep* 2:60
31. Rauscher I, Eiber M, Ganter C et al (2014) Evaluation of T1rho as a potential MR biomarker for liver cirrhosis: comparison of healthy control subjects and patients with liver cirrhosis. *Eur J Radiol* 83:900–904
32. Singh A, Reddy D, Haris M et al (2015) T1rho MRI of healthy and fibrotic human livers at 1.5 T. *J Transl Med* 13:292
33. Wang YX, Yuan J (2014) Evaluation of liver fibrosis with T1rho MR imaging. *Quant Imaging Med Surg* 4:152–155
34. Santyr GE, Henkelman RM, Bronskill MJ (1989) Spin locking for magnetic resonance imaging with application to human breast. *Magn Reson Med* 12:25–37
35. Huber S, Muthupillai R, Lambert B et al (2006) Tissue characterization of myocardial infarction using T1rho: influence of contrast dose and time of imaging after contrast administration. *J Magn Reson Imaging* 24:1040–1046
36. Muthupillai R, Flamm SD, Wilson JM et al (2004) Acute myocardial infarction: tissue characterization with T1rho-weighted MR imaging — initial experience. *Radiology* 232:606–610
37. Chavhan GB, Alsabban Z, Babyn PS (2014) Diffusion-weighted imaging in pediatric body MR imaging: principles, technique, and emerging applications. *Radiographics* 34:E73–E88
38. Michailovich O, Rathi Y, Dolui S (2011) Spatially regularized compressed sensing for high angular resolution diffusion imaging. *IEEE Trans Med Imaging* 30:1100–1115
39. Ning L, Setsompop K, Michailovich O et al (2015) A compressed-sensing approach for super-resolution reconstruction of diffusion MRI. *Inf Process Med Imaging* 24:57–68
40. Taouli B, Beer AJ, Chenevert T et al (2016) Diffusion-weighted imaging outside the brain: consensus statement from an ISMRM-sponsored workshop. *J Magn Reson Imaging* 44:521–540
41. Setsompop K, Cohen-Adad J, Gagoski BA et al (2012) Improving diffusion MRI using simultaneous multi-slice echo planar imaging. *Neuroimage* 63:569–580
42. Serai SD, Otero HJ, Calle-Toro JS et al (2019) Diffusion tensor imaging of the kidney in healthy controls and in children and young adults with autosomal recessive polycystic kidney disease. *Abdom Radiol* 44:1867–1872
43. Bakan AA, Inci E, Bakan S et al (2012) Utility of diffusion-weighted imaging in the evaluation of liver fibrosis. *Eur Radiol* 22:682–687
44. Partridge SC, McDonald ES (2013) Diffusion weighted magnetic resonance imaging of the breast: protocol optimization, interpretation, and clinical applications. *Magn Reson Imaging Clin N Am* 21:601–624
45. Galea N, Cantisani V, Taouli B (2013) Liver lesion detection and characterization: role of diffusion-weighted imaging. *J Magn Reson Imaging* 37:1260–1276
46. States LJ, Reid JR (2020) Whole-body PET/MRI applications in pediatric oncology. *AJR Am J Roentgenol* 215:713–725
47. Greer MC, Voss SD, States LJ (2017) Pediatric cancer predisposition imaging: focus on whole-body MRI. *Clin Cancer Res* 23:e6–e13
48. Bonekamp S, Corona-Villalobos CP, Kamel IR (2012) Oncologic applications of diffusion-weighted MRI in the body. *J Magn Reson Imaging* 35:257–279
49. Afaq A, Andreou A, Koh DM (2010) Diffusion-weighted magnetic resonance imaging for tumour response assessment: why, when and how? *Cancer Imaging* 10:S179–S188
50. Wu LM, Hu J, Gu HY et al (2013) Can diffusion-weighted magnetic resonance imaging (DW-MRI) alone be used as a reliable sequence for the preoperative detection and characterisation of hepatic metastases? A meta-analysis. *Eur J Cancer* 49:572–584